Label-free hyperspectral nonlinear optical microscopy of the biofuel micro-algae *Haematococcus Pluvialis*

Aaron M. Barlow,[1,2] Aaron D. Slepkov,[3,5] Andrew Ridsdale,[2] Patrick J. McGinn,[4] and Albert Stolow[1,2,*]

[1] *Department of Physics, University of Ottawa, Ottawa ON, Canada*
[2] *Security & Disruptive Technologies, National Research Council, 100 Sussex Dr., Ottawa ON, Canada*
[3] *Department of Physics & Astronomy, Trent University, Peterborough ON, Canada*
[4] *Algal Carbon Conversion Flagship Program, National Research Council, Halifax, N.S., Canada*
[5] *Co-corresponding author: aaronslepkov@trentu.ca*
*albert.stolow@nrc.ca

Abstract: We consider multi-modal four-wave mixing microscopies to be ideal tools for the *in vivo* study of carotenoid distributions within the important biofuel microalgae *Haematococcus pluvialis*. We show that hyperspectral coherent anti-Stokes Raman scattering (CARS) microscopy generates non-invasive, quantitative real-time concentrations maps of intracellular carotenoid distributions in live algae.

OCIS codes: (300.6230) Spectroscopy, coherent anti-Stokes Raman scattering; (300.6290) Spectroscopy, four-wave mixing; (180.4315) Nonlinear microscopy;(170.1530) Cell analysis; (170.1420) Biology.

References and links

1. W. M. Tolles, J. W. Nibler, J. R. McDonald, and A. B. Harvey, "A Review of the Theory and Application of Coherent Anti-Stokes Raman Spectroscopy (CARS)," Appl. Spectrosc. **31**(4), 253–271 (1977).
2. A. Zumbusch, G. R. Holtom, and X. S. Xie, "Three-dimensional vibrational imaging by coherent anti-Stokes Raman scattering," Phys. Rev. Lett. **82**(20), 4142–4145 (1999).
3. A. F. Pegoraro, A. Ridsdale, D. J. Moffatt, Y. Jia, J. P. Pezacki, and A. Stolow, "Optimally chirped multimodal CARS microscopy based on a single Ti:sapphire oscillator," Opt. Express **17**(4), 2984–2996 (2009).
4. E. O. Potma and X. S. Xie, "CARS microscopy for biology and medicine," Opt. Photonics News **15**(11), 40–45 (2004).
5. C. L. Evans and X. S. Xie, "Coherent Anti-Stokes Raman Scattering Microscopy: Chemical Imaging for Biology and Medicine," Annu Rev Anal Chem (Palo Alto Calif) **1**(1), 883–909 (2008).
6. Y. Wang, C.-Y. Lin, A. Nikolaenko, V. Raghunathan, and E. O. Potma, "Four-wave mixing microscopy of nanostructures," Adv. Opt. Photon. **3**(1), 1 (2011).
7. J. Renger, R. Quidant, N. v. Hulst, and L. Novotny, "Surface-Enhanced Nonlinear Four-Wave Mixing," Phys. Rev. Lett. **104**, 046803 (2010).
8. M. Danckwerts and L. Novotny, "Optical Frequency Mixing at Coupled Gold Nanoparticles," Phys. Rev. Lett. **98**(2), 026104 (2007).
9. L. Huang and J.-X. Cheng, "Nonlinear Optical Microscopy of Single Nanostructures," Annu. Rev. Mater. Res. **43**(1), 213–236 (2013).
10. M. R. Droop, "Conditions governing haematochrome formation and loss in the alga haematocuccus pluvialis flotow," Arch. Mikrobiol. **20**(4), 391–397 (1954).
11. T. W. Goodwin and M. Jamikorn, "Studies in carotenogenesis. 11. Carotenoid synthesis in the alga Haematococcus pluvialis," Biochem. J. **57**(3), 376–381 (1954).
12. S. Boussiba, "Carotenogenesis in the green alga Haematococcus pluvialis: Cellular physiology and stress response," Physiol. Plant. **108**(2), 111–117 (2000).
13. L. Fan, A. Vonshak, A. Zarka, and S. Boussiba, "Does astaxanthin protect Haematococcus against light damage?" Z. Naturforsch., C, J. Biosci. **53**(1-2), 93–100 (1998).
14. K. Grünewald, J. Hirschberg, and C. Hagen, "Ketocarotenoid biosynthesis outside of plastids in the unicellular green alga *Haematococcus pluvialis*," J. Biol. Chem. **276**(8), 6023–6029 (2001).
15. M. Guerin, M. E. Huntley, and M. Olaizola, "Haematococcus astaxanthin: applications for human health and nutrition," Trends Biotechnol. **21**(5), 210–216 (2003).
16. K. Tominaga, N. Hongo, M. Karato, and E. Yamashita, "Cosmetic benefits of astaxanthin on humans subjects," Acta Biochim. Pol. **59**(1), 43–47 (2012).

17. J.-P. Yuan, J. Peng, K. Yin, and J.-H. Wang, "Potential health-promoting effects of astaxanthin: A high-value carotenoid mostly from microalgae," Mol. Nutr. Food Res. **55**(1), 150–165 (2011).
18. M. C. Damiani, C. A. Popovich, D. Constenla, and P. I. Leonardi, "Lipid analysis in Haematococcuspluvialis to assess its potential use as a biodiesel feedstock," Bioresour. Technol. **101**(11), 3801–3807 (2010).
19. C. Castiglioni, M. Del Zoppo, and G. Zerbi, "Vibrational Raman spectroscopy of polyconjugated organic oligomers and polymers," J. Ram **24**(8 Spec.), 485–494 (1993).
20. Z. Pilát, S. Bernatová, J. Ježek, M. Šerý, O. Samek, P. Zemánek, L. Nedbal, and M. Trtílek, "Raman microspectroscopy of algal lipid bodies: β-carotene quantification," J. Appl. Phycol. **24**(3), 541–546 (2012).
21. A. Kaczor, K. Turnau, and M. Baranska, "In situ Raman imaging of astaxanthin in a single microalgal cell," Analyst (Lond.) **136**(6), 1109–1112 (2011).
22. A. M. Collins, H. D. T. Jones, D. Han, Q. Hu, T. E. Beechem, and J. A. Timlin, "Carotenoid Distribution in Living Cells of Haematococcus pluvialis (Chlorophyceae)," PLoS ONE **6**(9), e24302 (2011).
23. M. Wayama, S. Ota, H. Matsuura, N. Nango, A. Hirata, and S. Kawano, "Three-Dimensional Ultrastructural Study of Oil and Astaxanthin Accumulation during Encystment in the Green Alga Haematococcus pluvialis," PLoS ONE **8**(1), e53618 (2013).
24. C. Brackmann, A. Bengtsson, M. L. Alminger, U. Svanberg, and A. Enejder, "Visualization of beta-carotene and starch granules in plant cells using CARS and SHG microscopy," J. Ram **42**(4 Spec.), 586–592 (2011).
25. H. Kano and H. Hamaguchi, "Vibrationally resonant imaging of a single living cell by supercontinuum-based multiplex coherent anti-Stokes Raman scattering microspectroscopy," Chem. Lett. **35**, 1124–1125 (2006).
26. A. Dementjev and J. Kostkevičiene, "Applying the method of Coherent Anti-stokes Raman microscopy for imaging of carotenoids in microalgae and cyanobacteria," J. Ram **44**(7 Spec.), 973–979 (2013).
27. X. N. He, J. Allen, P. N. Black, T. Baldacchini, X. Huang, H. Huang, L. Jiang, and Y. F. Lu, "Coherent anti-Stokes Raman scattering and spontaneous Raman spectroscopy and microscopy of microalgae with nitrogen depletion," Biomed. Opt. Express **3**(11), 2896–2906 (2012).
28. P. Mahou, N. Olivier, G. Labroille, L. Duloquin, J.-M. Sintes, N. Peyriéras, R. Legouis, D. Débarre, and E. Beaurepaire, "Combined third-harmonic generation and four-wave mixing microscopy of tissues and embryos," Biomed. Opt. Express **2**(10), 2837–2849 (2011).
29. P. D. Maker and R. W. Terhune, "Study of Optical Effects Due to an Induced Polarization Third Order in the Electric Field Strength," Phys. Rev. **137**(3A), A801–A818 (1965).
30. M. Cui, B. R. Bachler, and J. P. Ogilvie, "Comparing coherent and spontaneous Raman scattering under biological imaging conditions," Opt. Lett. **34**(6), 773–775 (2009).
31. J.-X. Cheng and X. S. Xie, "Coherent Anti-Stokes Raman Scattering Microscopy: Instrumentation, Theory, and Applications," J. Phys. Chem. B **108**(3), 827–840 (2004).
32. J.-X. Cheng, L. D. Book, and X. S. Xie, "Polarization coherent anti-Stokes Raman scattering microscopy," Opt. Lett. **26**(17), 1341–1343 (2001).
33. E. O. Potma, C. L. Evans, and X. S. Xie, "Heterodyne coherent anti-Stokes Raman scattering (CARS) imaging," Opt. Lett. **31**(2), 241–243 (2006).
34. Y. Liu, Y. J. Lee, and M. T. Cicerone, "Broadband CARS spectral phase retrieval using a time-domain Kramers-Kronig transform," Opt. Lett. **34**(9), 1363–1365 (2009).
35. E. M. Vartiainen, H. A. Rinia, M. Müller, and M. Bonn, "Direct extraction of Raman line-shapes from congested CARS spectra," Opt. Express **14**(8), 3622–3630 (2006).
36. F. Masia, A. Glen, P. Stephens, P. Borri, and W. Langbein, "Quantitative Chemical Imaging and Unsupervised Analysis Using Hyperspectral Coherent Anti-Stokes Raman Scattering Microscopy," Anal. Chem. **85**(22), 10820–10828 (2013).
37. A. F. Pegoraro, A. D. Slepkov, A. R. Ridsdale, D. J. Moffatt, and A. Stolow, "Hyperspectral multimodal CARS microscopy in the fingerprint region," J. Biophotonics **7**(1-2), 49–58 (2014).
38. A. D. Slepkov, A. M. Barlow, A. R. Ridsdale, P. J. McGinn, and A. Stolow, "In vivo hyperspectral CARS and FWM microscopy of carotenoid accumulation in *H. Pluvialis*," Proc. SPIE 8937, Multimodal Biomedical Imaging **IX**, 893709 (2014).
39. T. Hellerer, A. M. K. Enejder, and A. Zumbusch, "Spectral focusing: High spectral resolution spectroscopy with broad-bandwidth laser pulses," Appl. Phys. Lett. **85**(1), 25–27 (2004).
40. I. Rocha-Mendoza, W. Langbein, and P. Borri, "Coherent anti-Stokes Raman microspectroscopy using spectral focusing with glass dispersion," Appl. Phys. Lett. **93**(20), 201103 (2008).
41. R. K. Lyn, D. C. Kennedy, S. M. Sagan, D. R. Blais, Y. Rouleau, A. F. Pegoraro, X. S. Xie, A. Stolow, and J. P. Pezacki, "Direct imaging of the disruption of hepatitis C virus replication complexes by inhibitors of lipid metabolism," Virology **394**(1), 130–142 (2009).
42. Y. Fu, H. Wang, R. Shi, and J.-X. Cheng, "Characterization of photodamage in coherent anti-Stokes Raman scattering microscopy," Opt. Express **14**(9), 3942–3951 (2006).
43. A. G. Christophersen, H. Jun, K. Jørgensen, and L. H. Skibsted, "Photobleaching of astaxanthin and canthaxanthin," Z. Lebensm. Unters. Forsch. **192**(5), 433–439 (1991).
44. H.-M. Chen and S. P. Meyers, "A rapid quantitative method for determination of astaxanthin pigment concentration in oil extracts," J. Am. Oil Chem. Soc. **61**(6), 1045–1047 (1984).
45. L. Rimai, M. E. Heyde, and D. Gill, "Vibrational spectra of some carotenoids and related linear polyenes. Raman spectroscopic study," J. Am. Chem. Soc. **95**(14), 4493–4501 (1973).

46. Y. Koyama, M. Kuki, P. O. Andersson, and T. Gillbro, "Singlet Excited States and the Light-Harvesting Function of Carotenoids in Bacterial Photosynthesis," Photochem. Photobiol. **63**(3), 243–256 (1996).

1. Introduction

Four-wave mixing microscopies are a suite of imaging techniques that employ third order nonlinear optical effects to generate contrast based on the interaction strength between four light fields within a specimen. Perhaps the most well-known of these techniques is coherent anti-Stokes Raman scattering (CARS) microscopy, a vibrationally resonant four-wave mixing analogue of Raman scattering that allows for rapid imaging with vibrational mode contrast [1–5]. CARS microscopy is most commonly employed for the study of biomedical systems through the many well-known intense Raman resonances found in biological molecules. There is also considerable interest in a related (vibrationally-) nonresonant four-wave mixing (FWM) process. FWM microscopy is particularly useful for inorganic systems including metal surfaces, semiconductors, and quantum dots [6–9]. This technique exploits the intrinsic (electronic) nonlinear optical susceptibility of materials to generate contrast and, hence, does not require the presence of any vibrational resonances. In practice, however, enhancement through plasmonic or electronic resonances is greatly preferred [6]. These nonlinear optical techniques possess several key attributes: high-sensitivity; chemical specificity; and rapid non-destructive three-dimensional live cell imaging in biological systems. Here, we demonstrate the effectiveness of both CARS and FWM nonlinear microscopies as label-free imaging modalities for the *in vivo* study of carotenoids, shown for the commercially important microalgae *Haematococcus pluvialis*.

H. pluvialis are a species of flagellated green microalgae found in freshwater ponds and rainwater pools virtually worldwide [10]. Upon exposure to environmental stress, these algae synthesize large amounts of the ketocarotenoid astaxanthin (AXN) within lipid droplets, causing them to swell into cysts several times their original size [11–14]. AXN is a powerful antioxidant with a variety of reported health benefits and is used to make dyes, cosmetics, nutritional supplements, and food additives, with current annual world-wide sales exceeding a hundred million dollars [15–17]. Furthermore, the increased lipid production associated with the transition between the motile and cyst morphologies renders *H. pluvialis* an important candidate source for biofuels [18].

Due to this significant commercial interest in AXN, there is ongoing research aimed at understanding and quantifying carotenogenesis in *H. pluvialis*. Carotenoids have very large Raman cross-sections [19,20], engendering several confocal Raman microscopy studies to image carotenoid distributions within microalgae [20,21], and to map the conversion of *β*-carotene to AXN through the algal life cycle [22]. With complementary techniques such as transmission electron microscopy, the intracellular morphologies at key points in the algal life cycle have recently been mapped. Transmission electron microscopy has demonstrated that the degradation of the chloroplast is concurrent with AXN production [23]. Imaging modalities based on four-wave mixing offer an ideal bridge between Raman and electron microscopies, allowing for *in vivo* label-free imaging and quantitative assaying of intracellular carotenoid at rates and sensitivities superior to spontaneous Raman scattering, while avoiding the invasiveness, lack of chemical specificity and technical challenges of transmission electron microscopy [24–27].

Here we report that AXN distributions in *H. pluvialis* can be imaged efficiently using either CARS or FWM with simultaneous collection of two-photon excited fluorescence (TPEF), the latter permitting mapping of the intracellular chlorophyll content. This can be achieved in two distinct pump wavelength regimes, meaning that independent CARS and FWM images can be obtained. With lower pump frequency input ($\omega_1 \approx 11000$ cm^{-1}), we generate resonant-signal-dominated (i.e. nearly background-free) hyperspectral CARS images of AXN *in vivo*. Alternately, with higher pump frequencies ($\omega_1 \approx 12200$ cm^{-1}), we can image directly with FWM without any significant vibrational contribution. This is amongst the first

demonstrations of label-free electronic FWM microscopy applied to a native biological system [28]. Both CARS and FWM generate very large signals from AXN, enabling calibrated, high sensitivity measurements of intracellular concentrations, producing high-resolution, non-destructive, rapid, and label-free *in vivo* images of *H. pluvialis* with minimal sample preparation.

2. Theory

CARS uses two laser fields, traditionally called the pump (ω_1) and Stokes (ω_2), tuned such that their difference frequency matches a Raman-active molecular vibrational resonance (Ω). The nonlinear mixing process generates a blue-shifted anti-Stokes (ω_4) field as shown schematically in Fig. 1(a) (in most CARS schemes, the "probe" field is degenerate in the pump, i.e. $\omega_1 = \omega_3$) [29]. Like Raman scattering, CARS is label-free and chemically specific. However, because of its stimulated rather than spontaneous nature, CARS signal intensities can be several orders of magnitude stronger than those from spontaneous Raman scattering [1,30]. The tight focus excitation scheme of the nonlinear optical CARS process allows for inherently confocal three-dimensional images to be produced, where each pixel contains a vibrational Raman spectrum of the sample—so called hyperspectral imaging [2–5].

One of the main challenges associated with CARS microscopy is the presence of a ubiquitous background signal resulting from simultaneous electronic FWM in the sample (see scheme in Fig. 1(b)). FWM uses the same excitation fields as CARS, ω_1, ω_2, ω_4; however, rather than involving a vibrational resonance at second order, FWM depends only on the electronic third-order susceptibility $\chi^{(3)}$ within the sample under investigation. Since both processes are generated coherently within the focal volume, the forward propagating signals interfere with each other at the detector, producing well known spectral distortions in CARS spectroscopy. Consequently, there has been considerable effort in the CARS microscopy literature to develop methods that suppress the FWM signal [31–33] or to deconvolve the CARS spectrum from this non-resonant "background" [34–36]. In either case, the extracted resonant spectrum provides essentially the same information as does the spontaneous Raman spectrum [1].

We note that FWM may also be used directly as a method for imaging. Unlike CARS, the FWM signal is insensitive to vibrational resonances and rather relies on variations in electronic $\chi^{(3)}$ for image contrast. While this means that the FWM signal will not have detailed spectral fingerprinting, it is also relatively insensitive to the precise frequency difference $\omega_1 - \omega_2$, and is thus less restrictive in laser wavelength tunability, meaning that imaging can be achieved with a simple instrument.
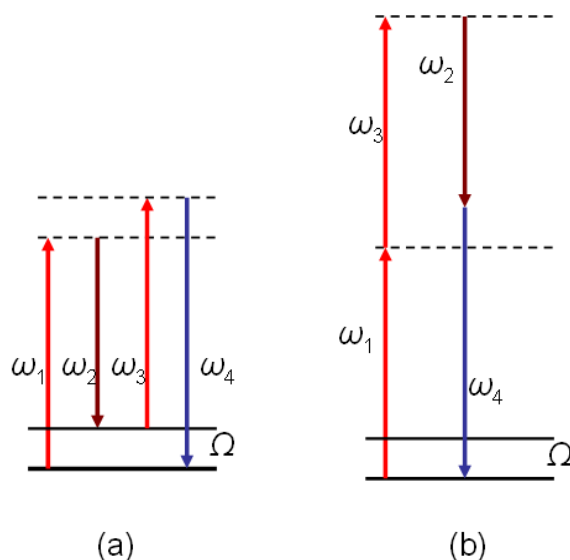
Fig. 1. Energy level diagrams for four-wave mixing processes with pump at frequency ω_1, Stokes at frequency ω_2, probe frequency ω_3 and anti-Stokes at frequency ω_4. (a) Coherent anti-Stokes Raman scattering, vibrationally resonant with a Raman transition of frequency Ω. (b) Non-resonant four-wave mixing. In these experiments, $\omega_1 = \omega_3$.

3. Experimental design

Our microscopy setup and implementation of broadband CARS hyperspectral microscopy is described in detail elsewhere [3,37,38]. An 80 MHz fs oscillator generates laser pulses with central wavelengths tunable between 790–930 nm (10800-12600 cm^{-1}), and a bandwidth of approx. 250 cm^{-1}. These pulses act as the 'pump' ω_1 in the CARS and FWM schemes. A fraction of this light is used to generate a red-shifted supercontinuum spanning 950–1250 nm (8000–10500 cm^{-1}) using a two-zero dispersion point photonic crystal fiber (FemtoWhite CARS). This acts as ω_2 ('Stokes') in the CARS and FWM schemes. Both the pump and supercontinuum are temporally stretched (chirped) at the same rate before being recombined and sent into the microscope. The chirp rates for this instrument are in the range of 0.17–0.21 cm^{-1}/fs, yielding a spectral resolution of order 30 cm^{-1}. When needed, this resolution is improved significantly (e.g. to ~5 cm^{-1}) by increasing the pulse chirp rate, albeit at the expense of signal intensity [39,40]. This method, called 'spectral focusing', leads to a narrowband CARS resonance by creating a constant frequency difference between the two laser fields [39]. The central frequency and bandwidth of this slice is governed by the timing and pulse duration of ω_1. Simply by changing the time delay between the pump and supercontinuum Stokes, we can rapidly tune the instantaneous interaction frequency of ω_2, and, consequently, their frequency difference (i.e. scanning the Raman spectrum). In particular, when the pump laser is tuned between 870–930 nm, the frequency difference ω_1–ω_2 lies within the "fingerprint" spectral region spanning from 900–1900 cm^{-1}. Alternately, when the pump laser is tuned between 790–850 nm, the difference frequency spans the range 1700–4000 cm^{-1}. This also fixes the frequency of the detected light ω_4, which is collected in the forward direction in the range of 650–840 nm depending on the input pump power and Stokes frequency, and can be discriminated from the pump and fluorescence by bandpass filters. While this approach allows for a rapid spectral scanning, a significant drawback is that the supercontinuum output power is spectrally non-uniform. This complicates, for example, the quantitative determination of the ratio of intensities of two different peaks in the CARS

spectrum. In the case of FWM, the spectral non-uniformity of the supercontinuum results in a frequency dependence in the intensity of ω_4. However, this dependence is not associated with vibrational or electronic energy levels, but rather with spectral variations in the supercontinuum.

As discussed above, for the case of AXN, selecting a longer pump wavelength allows for fingerprint CARS imaging whereas a shorter pump wavelength regime yields dominant FWM signals. We note that the signals from AXN are much stronger than those from lipid samples commonly studied in CARS microscopy: Pump laser powers of 15−25 mW (at the sample) are typically required for CARS imaging of lipids in our system [41] whereas AXN can be easily visualized using CARS at 1.5 mW or with FWM at 0.5 mW pump power, in either case using only 2−3 mW of broadband Stokes supercontinuum. Considering that both of these nonlinear optical processes depend quadratically on the pump power, this implies that *in vivo* AXN has at least two orders of magnitude higher signal intensity—in either modality—than do pure lipids. Our estimates suggest AXN may have a per molecule response nearly six orders of magnitude greater than that of lipids (e.g. the C−H stretch in DMSO) [38]. The ability to characterize *in vivo* AXN distributions at very low laser powers is important because of sample photodegradation. In our experiments, *in vivo* photobleaching of AXN was noticeable with as little as 5 mW of pump power. The photobleaching in CARS and FWM signals scale nonlinearly with the peak laser power and pump wavelength [42], resulting in dramatic declines in CARS or FWM response at laser powers exceeding 10 mW. There is a concurrent degradation in the visible red pigmentation associated with AXN in the alga, consistent with studies on photobleaching of astaxanthin demonstrating that the photo-conversion manifests by a loss of absorption at the 488 nm peak [43].

Three-dimensional sectioning was achieved by scanning the microscope focus in the axial (*z*) dimension, while rapidly collecting an *x-y* image at each focal plane, with a typical axial resolution of ~2µm. The transverse (*x-y*) resolution was typically ~0.5 µm. TPEF generated in the range from 350−700 nm was simultaneously collected in the *epi*-direction.

The algae were grown in Bold's basal media with 3 × the normal nitrate supplementation at 22 °C under 150 µmol photons m^{-2} s^{-1} photosynthetically active radiation (PAR) and agitated on a shaking table at 175 rpm. To induce cyst development and AXN accumulation from vegetative green cells, the cultures were shifted to 800 µmol photons m^{-2} s^{-1} PAR for a few days as the cells entered the late log growth phase and nutrients became depleted. Samples of the algae in water were placed in a well slide at the microscope focus; no other preparation was necessary for imaging. A sample of AstaREAL-10L® (a commercially-available extract of esterified astaxanthin from *H. pluvialis,* nominally 10% AXN by weight) was used to calibrate the CARS signal intensity. This provided an excellent reference because its concentrated esterified AXN is in the same form and similar environment to that in live *H. pluvialis* cells. A known weight of AstaREAL was dissolved in canola oil via vigorous mixing, and a dilution series was created from this stock solution, with concentrations ranging from 45 to 2 mM. The solution concentrations were verified using known UV-Vis extinction coefficients of AXN from the literature [44].

4. Results and discussion

In Fig. 2, we show a composite image of several *H. pluvialis* cysts using CARS (red) and TPEF (green). The high-resolution (512 × 512 pixels with ~0.5 µm transverse resolution, ~1.5 µm axial resolution, and 2 µs pixel dwell time) images enable us to see the distribution of AXN within the cell for various cellular morphologies. At each CARS frequency, an image is generated in less than one second. An entire hyperspectral scan is collected in a few minutes. It can be seen that the TPEF and CARS signals are strongly anti-correlated, representing distinct spatial regions within the cell. The CARS signal, which maps the AXN content, is confined to small, well-defined regions—presumably lipid drops—near the interior of the

cell. These are surrounded by chloroplasts that are simultaneously visualized by TPEF. A few cells exhibited significant reduction of chlorophyll signals, and, for these, the entire cell was dominated by large AXN deposits, confirming that AXN biosynthesis ultimately comes at the expense of chlorophyll [23].
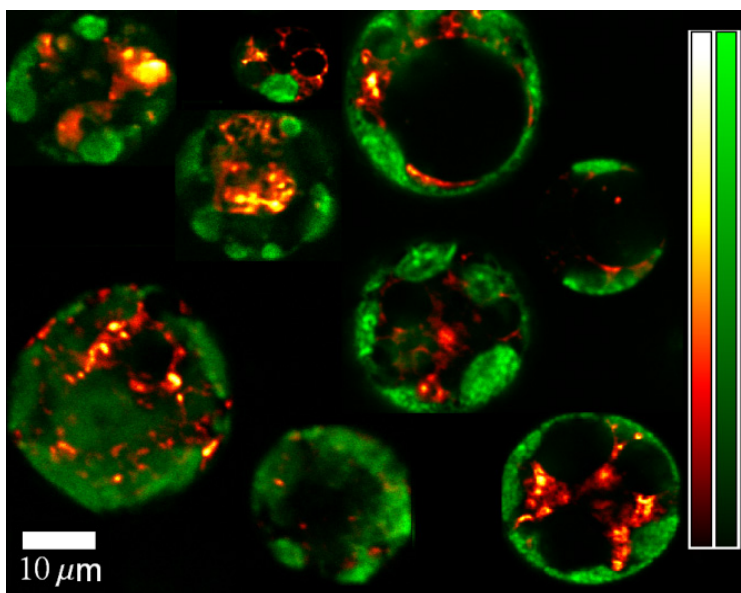

Fig. 2. Composite image of various *H. pluvialis* cells using forward-collected CARS from AXN at 1520 cm^{-1} (red) and epi-collected TPEF from chlorophyll (green). The cells show several distinctive morphologies, ranging from minimal AXN content within a chlorophyll-dominated cell, to those with several AXN-containing droplets, to cells where AXN almost completely dominates the interior of the cell. Several cells also appear to have large transparent voids within them.

In Fig. 3, we show a three-dimensional reconstruction of a cell made from images taken in 1-μm z-steps (Media 1), showing the spatial distribution of cellular contents throughout the whole volume. Again, a near-complete segregation of the chlorophyll and AXN is observed, with a dense deposit of AXN dominating the interior of the cell, enclosed by a thin exterior layer of chlorophyll.

In addition to spatial localization of cellular constituents by CARS vibrational contrast imaging, our technique allows for facile hyperspectral mapping by rapidly scanning the CARS spectrum. In Fig. 4(b), we show the CARS spectrum from the highlighted region of interest in Fig. 4(a). We can identify several peaks in the CARS spectrum, with major features at 1150 cm^{-1} and 1520 cm^{-1} and several minor peaks in the intermediate region between them. These prominent peaks are identified as being associated, respectively, with C—C, and C = C stretching vibrations characteristic of carotenoids [45]. The peak near 1007 cm^{-1} associated with C—CH$_3$ stretching is not observed at this pump wavelength due to a lack of power in the corresponding Stokes spectrum at a wavelength of 1000 nm, but is easily observed with a lower-power generation of the Stokes supercontinuum [38]. Overlaid with these are the peaks taken from the spontaneous Raman spectrum of AstaREAL. There is excellent agreement between the two, especially when the spontaneous Raman is broadened to our instrumental spectral resolution of 30 cm^{-1}. The CARS spectrum of AXN does not exhibit any of the distortions typical of CARS spectroscopy. None of the typical post-processing was required for direct comparison to the spontaneous Raman spectrum [34,35]. This is due to the fact that, at the 915 nm pump wavelength used in the fingerprint region, the CARS intensity from AXN is several orders of magnitude larger than the FWM signal. In

other words, there is disproportionately little non-resonant background signal to interfere with the resonant CARS signal.
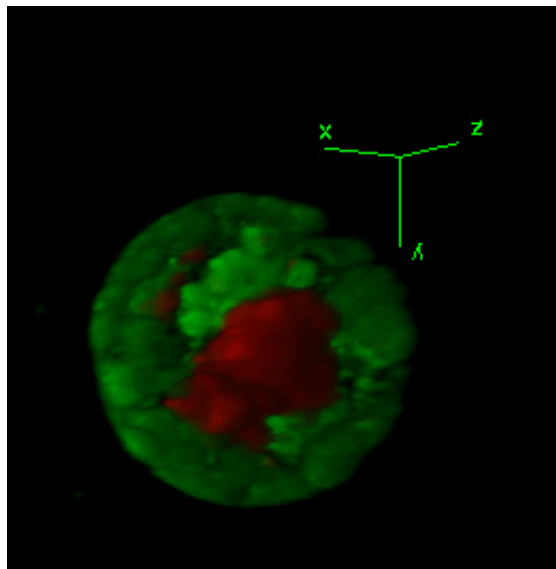

Fig. 3. 3D projection of *H. pluvialis* cell using forward-collected CARS (red) and epi-directed TPEF (green). (Media 1)

The intensity of the *in vivo* CARS response is remarkably large and dwarfs those of common calibration standards, such as diamond (at 1335 cm^{-1}), by two orders of magnitude or more. We are currently investigating the mechanism underlying this enhancement. A simple electronic resonance enhancement can be ruled out because none of the pump, probe, or Stokes frequencies are resonant with an electronic energy level in AXN. Furthermore, a third- order electronic resonance (i.e. at the anti-Stokes frequency $2\omega_1 - \omega_2$) is still at an energy far below the relevant known electronic states in AXN. The longest wavelength absorption (from the ground state) is the S0→S2 transition at 480 nm, at least 8400 cm^{-1} to the blue of the 803 nm anti-Stokes frequency [46]. The S0→S1 transition (nominally 750 nm, 13300 cm^{-1}) is nominally one-photon parity forbidden and therefore can only weakly interact via vibronic-coupling induced (e.g. Herzberg-Teller) intensity borrowing mechanisms. Based on the measured UV-Vis spectrum of the AstaREAL, we can conclude the oscillator strength for the S0→S1 transition is at least four orders of magnitude weaker than the S0→S2 transition, so any resonant contribution from this state would be correspondingly small [38]. The origin of this enhancement may yet involve such pre-resonant Raman effects and remains the subject of our ongoing investigations.
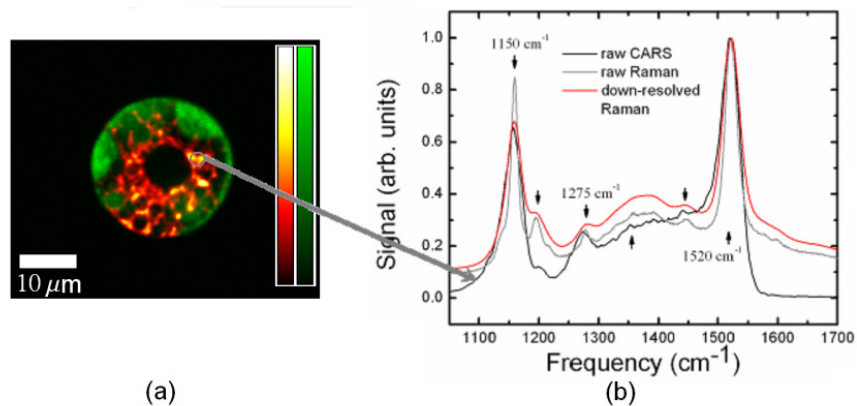
Fig. 4. (a) Hyperspectral CARS/TPEF image of an algal cell at a Raman shift of 1520 cm^{-1}. (b) Black: Raw CARS spectrum extracted from the highlighted region. Grey: Spontaneous Raman spectrum of AstaREAL standard collected with a Raman spectrometer. Red: The same Raman spectrum after being broadened to the CARS spectral resolution of 30 cm^{-1}.

By tuning the pump laser to the 780 nm–840 nm region, we can image *H. pluvialis* using FWM rather than CARS, as shown in Fig. 5. A motile (flagellated) alga is shown in Fig. 5(a), whose motion can be tracked at a 0.44 fps frame rate in a 256×256 field (Media 2). Somewhat surprisingly, this alga appears to contain a small pocket of carotenoid at its center, despite the fact that AXN production in significant quantities is generally only associated with encystment [23]. The image contrast for the cysts, as shown in Fig. 5(b), is comparable in FWM to that seen with CARS. In Fig. 5(c) we show the FWM response as a function of the frequency difference $\omega_1 - \omega_2$ (green) overlaid with the Stokes spectrum (blue). While the FWM spectrum does display some structure, as noted above, the structure is not associated with resonances in AXN, but rather is proportional to the power-spectral-density of the measured spectrum of the Stokes supercontinuum. Affirming this, it can be seen that the spectral features in the FWM signal are considerably broader than the vibrationally resonant features in the spontaneous Raman spectrum of AstaREAL (red) and do not correspond to known vibrational resonances. Since the signal nonetheless is produced at the appropriate "anti-Stokes" frequencies and shows the appropriate power scaling dependence on both pump and Stokes, we assign this signal to FWM. We do not see the C–H vibrational resonance characteristic of lipid drops at 2850 cm^{-1}; the FWM response overwhelms that of the vibrationally resonant lipids.

As with the case of the fingerprint-region CARS response, there appears to be significant enhancement of the FWM signal intensity compared to typical non-resonant background signals seen in CARS microscopy. We are presently unable to assign this enhancement to any known one- or two-photon-allowed electronic transitions in AXN. In Fig. 5(d), we show the spectrum in a "transition region" between the FWM and CARS regimes at 860 nm, where, in this case, the intensities have been normalized to the Stokes spectrum. The CARS signal is approximately seven times larger than that of the FWM in this region, and there is possibly some indication of spectral reshaping on the blue side of the CARS peak. The FWM enhancement does not, however, appear to extend to the 870 nm – 930 nm range, since it is not seen to interfere with the fingerprint CARS response as seen in Fig. 4(b): The FWM response appears to diminish rapidly with wavelengths longer than 860 nm.

As expected for coherent nonlinear signals generated in a sample for which the vibrationally resonant signal dominates over the nonresonant background [1], the CARS signal depends quadratically on the concentration of AXN in the AstaREAL standard, as shown in Fig. 6(a). By comparing the generated CARS signal at 1520 cm^{-1} within the algae to

a known concentration of AstaREAL at the same Raman shift, we are able to quantify our signal intensities using an absolute concentration scale. This strict quadratic dependence holds even to our lowest measured concentration of 2 mM AXN in canola oil where we can still acquire well-resolved CARS spectra with little nonresonant background contribution (Fig. 6(b)).
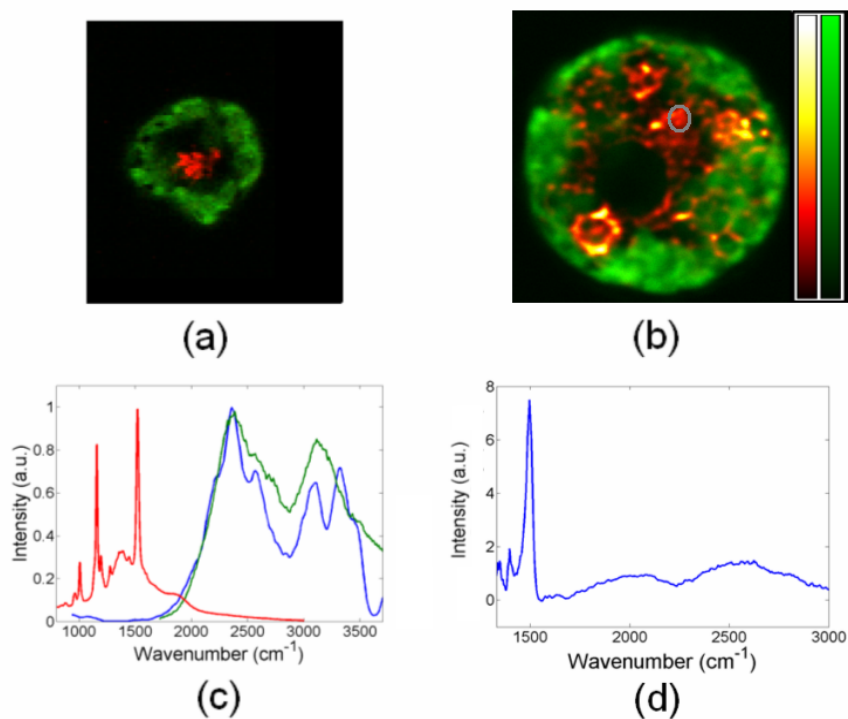

Fig. 5. (a) A frame of the motion of a flagellated *H. pluvialis* cell. The FWM signal is shown in red, the TPEF shown in green. (b) The imaging of an *H. pluvialis* cyst using FWM. (c) The frequency difference $\omega_1 - \omega_2$ of the FWM of the highlighted region of (b), shown in green. The frequencies generated by the Stokes supercontinuum (downwards shifted by 7900 cm^{-1} for overlay purposes) are shown in blue. For comparison, the spontaneous Raman spectrum collected at 785 nm of AstaREAL is plotted in red. (d) The CARS/FWM spectrum of AstaREAL at 860 nm, normalized by the Stokes spectrum. Features below ~1500 cm^{-1} cannot be resolved due to a lack of Stokes power at these frequencies. (See Media 2)
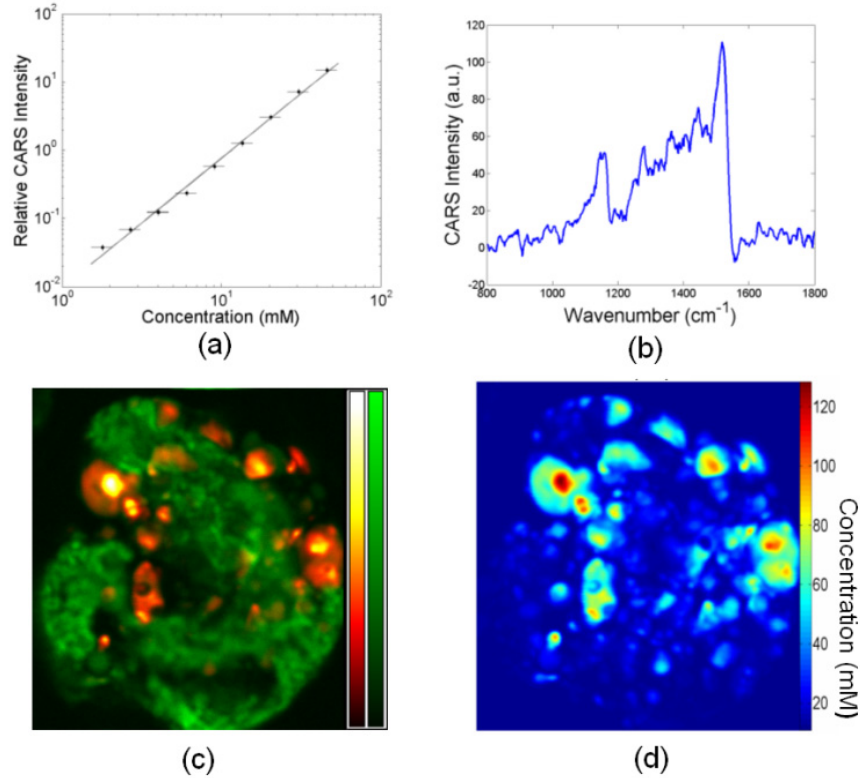
Fig. 6. (a) Log-log plot of CARS signal intensity vs. AXN concentration in canola oil, showing a quadratic (slope = 1.94) dependence. (b) (electronic offset baseline-subtracted) CARS spectrum of AXN at 2 mM concentration. (c) CARS (red) / TPEF (green) image of a particular algal cell at a Raman shift of 1520 cm^{-1}. (d) A concentration map of AXN within the cell depicted in (c). The scale bar colour map has units of mM AXN.

Given the high signal-to-noise and minimal signal averaging required to generate this spectrum, we anticipate a detection limit for carotenoids well below the millimolar level. Using this concentration calibration, we are able to transform the CARS image of the algal cell in Fig. 6(c) into an *in vivo* concentration map, as shown in Fig. 6(d). We observe intracellular AXN concentrations up to 120 ± 10 mM and note that AXN content is minimal in the regions of the chloroplast. From our AstaREAL dilutions, we estimate that AXN concentrations saturate in lipid droplets at $150–180 \pm 20$ mM, suggesting that the most abundant cellular regions are nearly saturated. It should be noted that FWM also varies quadratically with concentration, so identical concentration quantifications can be performed using either CARS or FWM.

5. Conclusions

CARS and FWM offer several distinct advantages for the *in vivo* analysis of *H. pluvialis*. Much like spontaneous Raman, these techniques are able to chemically identify AXN within living cells. However, whereas fluorescence is typically an undesirable background in Raman microscopy, here we use (TPEF) fluorescence as an additional contrast mechanism, allowing simultaneous determination of both chlorophyll and AXN distributions. The large CARS and FWM signals allow for high resolution spectrally-resolved images to be generated in only a few minutes. For researchers whose primary interest is in imaging carotenoids or assaying their concentrations, FWM provides an experimentally simple means for doing so. Since it can be accessed using the standard 800 nm Ti:Sa laser wavelength and has a relatively

relaxed dependence on ω_2, FWM microscopy can be immediately attained by adding a commercial CARS module to a standard two-photon microscopy system with minimal technical challenges. On the other hand, researchers wishing for the added advantage of spectroscopy may choose to implement a fingerprint CARS system.

CARS and FWM microscopies offer distinct advantages over both transmission electron microscopy [22] and Raman microscopy [23,24] for the *in vivo* study of carotenoids. While the nonlinear modalities lack the spatial resolution of electron microscopy, CARS and FWM can be readily performed on live cells in aqueous solution with minimal sample preparation. Raman microscopy, on the other hand, can be performed on live cells with excellent spectral contrast, but its low signals and long integration times lead to poorer image quality, and cannot typically be used for real-time monitoring of cells. The intense signals afforded by CARS and FWM overcome the difficulties in either technique. CARS and FWM measurements may be conducted in real time with excellent contrast to track dynamic responses to stresses, and directly monitor the rate of carotenogenesis throughout the algal life cycle. Moreover, since three-dimensional sectioning with sub-micron resolution is inherent to these third order microscopy modalities, CARS and FWM allow for whole-volume *in vivo* studies of *H. pluvialis*, with vibrational spectral contrast and quantitative concentration analysis.

Acknowledgments